Acta Pharmaceutica Sinica B 2021;11(11):3636–3647

Chinese Pharmaceutical Association
Institute of Materia Medica, Chinese Academy of Medical Sciences

Acta Pharmaceutica Sinica B

www.elsevier.com/locate/apsb
www.sciencedirect.com

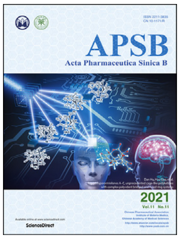

ORIGINAL ARTICLE

Pure photosensitizer-driven nanoassembly with core-matched PEGylation for imaging-guided photodynamic therapy

Shenwu Zhang[a], **Yuequan Wang**[a], **Zhiqiang Kong**[a], **Xuanbo Zhang**[a], **Bingjun Sun**[a], **Han Yu**[a], **Qin Chen**[b], **Cong Luo**[a,*], **Jin Sun**[a,*], **Zhonggui He**[a,*]

[a]*Department of Pharmaceutics, Wuya College of Innovation, Shenyang Pharmaceutical University, Shenyang 110016, China*
[b]*Department of Pharmacy, Cancer Hospital of China Medical University, Liaoning Cancer Hospital & Institute, Shenyang 110042, China*

Received 14 December 2020; received in revised form 10 March 2021; accepted 15 March 2021

KEY WORDS

Pure drug-assembled nanomedicines;
Pure photosensitizer;
Pyropheophorbide a;
Core-matched;
Self-assembly;
Nanoassembly;
Imaging-guided;
Photodynamic therapy

Abstract Pure drug-assembled nanomedicines (PDANs) are currently under intensive investigation as promising nanoplatforms for cancer therapy. However, poor colloidal stability and less tumor-homing ability remain critical unresolved problems that impede their clinical translation. Herein, we report a core-matched nanoassembly of pyropheophorbide a (PPa) for photodynamic therapy (PDT). Pure PPa molecules are found to self-assemble into nanoparticles (NPs), and an amphiphilic PEG polymer (PPa-PEG$_{2K}$) is utilized to achieve core-matched PEGylating modification *via* the $\pi-\pi$ stacking effect and hydrophobic interaction between the PPa core and the PPa-PEG$_{2K}$ shell. Compared to PCL-PEG$_{2K}$ with similar molecular weight, PPa-PEG$_{2K}$ significantly increases the stability, prolongs the systemic circulation and improves the tumor-homing ability and ROS generation efficiency of PPa-nanoassembly. As a result, PPa/PPa-PEG$_{2K}$ NPs exert potent antitumor activity in a 4T1 breast tumor-bearing BALB/c mouse xenograft model. Together, such a core-matched nanoassembly of pure photosensitizer provides a new strategy for the development of imaging-guided theragnostic nanomedicines.

Abbreviations: ACQ, aggregation caused quenching; ALT, alanine aminotransferase; AST, aspartate aminotransferase; BUN, blood urine nitrogen; CRE, creatinine; DCFH-DA, 2′,7′-dichlorofluorescein diacetate; DDS, drug delivery system; FBS, fetal bovine serum; NaCl, sodium chloride; nano-DDS, nanoparticulate drug delivery systems; NPs, nanoparticles; PBS, phosphate buffer solution; PDANs, pure drug-assembled nanomedicines; PDT, photodynamic therapy; PPa, pyropheophorbide a; PS, photosensitizer; ROS, reactive oxygen species; SDS, sodium dodecyl sulfate; SOSG, Singlet Oxygen Sensor Green Reagent.

*Corresponding authors.

E-mail addresses: luocong@syphu.edu.cn (Cong Luo), sunjin@syphu.edu.cn (Jin Sun), hezhgui_student@aliyun.com (Zhonggui He).

Peer review under responsibility of Chinese Pharmaceutical Association and Institute of Materia Medica, Chinese Academy of Medical Sciences.

https://doi.org/10.1016/j.apsb.2021.04.005

1. Introduction

Cancer is still considered as one of the most serious diseases threatening human health[1]. Currently, surgery is the most common and effective therapeutic approach for cancer, especially for the early stage of solid tumors without metastasis[2]. In addition to surgical removal of solid tumors, a variety of other treatment strategies have also been widely used in clinic, such as chemotherapy and phototherapy[3,4]. Among them, chemotherapy is the predominant therapeutic regimen for clinical treatment of cancer, especially for the patients with inoperable and massively metastatic tumors. However, serious toxicities are usually caused by systemic administration of chemotherapeutic agents, due to their narrow therapeutic windows and off-target distribution in the body[5]. Therefore, it is desirable that local diseases could be controlled and treated with site-specific local treatment regimens.

Compared with systemic chemotherapy, photodynamic therapy (PDT) has been widely investigated as a non-invasive cancer therapeutic approach[6]. Under tumor-localized laser irradiation, photosensitizers (PSs) induce the apoptosis and necrosis of tumor cells *via* producing large amounts of cytotoxic reactive oxygen species (ROS)[7,8]. The cytotoxic ROS damages the normal physiological functions of tumor cells by damaging the cell membrane and oxidizing the intracellular macromolecules[9−11]. Notably, PSs almost show no cytotoxicity without laser treatment, making phototherapy as favorable non-invasive treatment modality for site-specific cancer therapy[12]. Moreover, the clinical application of phototherapy has been extended to the treatment of tumors in the deep viscera, by virtue of the rapid development of novel PSs and fiber optic equipment[13]. However, the therapeutic efficacy of phototherapy is still impeded by the inefficient accumulation of PSs in tumors after intravenous administration[14]. Therefore, rational design of high-efficient drug delivery system (DDS) is of crucial importance for efficient phototherapy.

With the burgeoning biomedical nanotechnology, a variety of nanoparticulate drug delivery systems (nano-DDS) have been developed to improve the delivery efficacy of anticancer drugs, including PSs[15−21]. In particular, most PSs were non-covalently encapsulated in organic or inorganic nanocarriers for anticancer therapy[22−25]. Nevertheless, non-covalent drug loading approaches have long been criticized for low drug loading efficiency, poor stability, premature drug leakage, and potential carrier material-related toxicity[26]. Recently, pure drug-assembled nanomedicines (PDANs) of small-molecule drugs or prodrugs have emerged as a promising nanoplatform for efficient drug delivery[27−30]. Particularly, some hydrophobic drugs were found to be able to self-assemble into nanoparticles (NPs) by themselves[29−32]. However, PDANs usually show unsatisfactory colloidal stability, due to the relatively weak intermolecular interactions among small molecules.

Herein, we constructed a pure photosensitizer-driven nanoassembly with the feature of core-matched PEGylating stabilization for efficient PDT (Fig. 1). First, unique self-assembly phenomenon of a commonly-used photosensitizer (pyropheophorbide a, PPa) was observed. Moreover, an amphiphilic PEG polymer (PPa-PEG$_{2K}$) was ingeniously utilized to achieve core-matched PEGylating modification on the PPa-nanoassembly *via* hydrophobic and π–π stacking interaction between PPa and PPa-PEG$_{2K}$. Meanwhile, PCL-PEG$_{2K}$ with a very similar molecular weight was utilized as a control to demonstrate the advantage of core-matched and π–π stacking interaction between PPa and PPa-PEG$_{2K}$. The self-assembly mechanisms and core-matched interaction were investigated by molecular docking simulation. Additionally, sodium chloride (NaCl), sodium dodecyl sulfate (SDS) and urea were utilized to investigate self-assembly mechanisms of PPa-nanoassembly. These results demonstrated that multiple interactions and forces involved in the self-assembly process of PPa, and PEGylation modification significantly improved the colloidal stability of PPa-nanoassembly. Such a core-matched nanoassembly demonstrated multiple drug delivery advantages, including ultrahigh drug-loading capacity (74.8%, *w*/*w*), core-matched stability, prolonged systemic circulation, accelerated tumor accumulation, as well as favorable cellular uptake. These advantages resulted in significantly enhanced antitumor efficacy against BALB/c mice bearing 4T1 xenograft tumors. This is the first time that pure PPa is found to self-assemble into NPs, and the nanostructure with core-matched PEGylating modification could significantly facilitate the efficient delivery and the potent antitumor activity of the PPa-nanoassembly. Such a pure photosensitizer-driven and core-matched nanoassembly offers a promising application prospect for efficient imaging-guided PDT against cancer.

2. Materials and methods

2.1. Materials

PPa was purchased in Shanghai Dibo Biotechnology Co., Ltd. Cell culture medium, penicillin, streptomycin and fetal bovine serum (FBS) were all obtained from GIBCO, Invitrogen Corp. (Carlsbad, CA, USA). MTT, trypsin, Singlet Oxygen Sensor Green Reagent (SOSG) and Reactive Oxygen Species Assay Kit (DCFH-DA) were purchased from Dalian Meilun Biological Technology Co., Ltd. Hoechst 33342 was purchased from BD Biosciences. Cell culture consumables were purchased by Wuxi NEST Biotechnology Co., Ltd. PCL-PEG$_{2K}$ was obtained from Shanghai Ponsure Biological Technology Co., Ltd. PPa-PEG$_{2K}$ was obtained by our previous synthetic method[31]. Other reagents were of analytical grade.

2.2. Preparation of PPa nanoassemblies

The non-PEGylated and PEGylated PPa NPs (PPa/PCL-PEG$_{2K}$ NPs and PPa/PPa-PEG$_{2K}$ NPs) were prepared using a one-step nanoprecipitation method[32]. Briefly, PPa (1 mg) were dissolved in 200 μL of a mixed solution of tetrahydrofuran and ethanol (2:3, *v*/*v*). Then, the mixed solution was slowly added dropwise to 2 mL of water at a speed of 1200 rpm (Gongyi Yingyu Yuhua Instrument Factory, DF-101S, Shanghai, China). After stirring for 3 min, the organic reagents were removed by a vacuum rotary evaporator (YRE-5299, Yuhua, Gongyi, China) at room temperature. The final solution volume was made up to 2 mL. Similarly, the other two

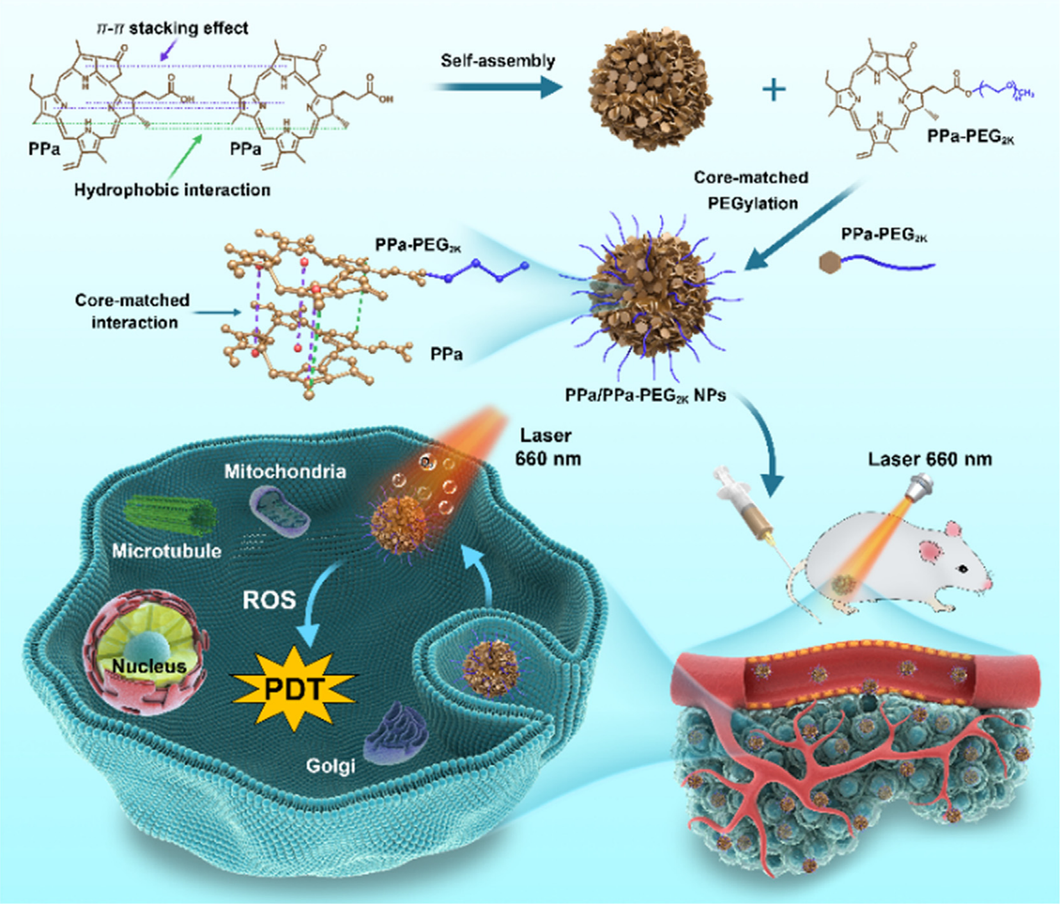

Figure 1 Schematic representation of self-assembly of PPa and efficient PDT under laser irradiation. Core-matched PPa nano-assembly was formed by the modification of PPa-PEG$_{2K}$. After PPa/PPa-PEG$_{2K}$ NPs are delivered to tumor tissues and endocytosed by tumor cells to exert effective photodynamic therapy under laser irradiation.

PEGylated nanosystems were prepared in the same procedure dissolving PPa with 10 mol% PCL-PEG$_{2K}$ or 10 mol% PPa-PEG$_{2K}$ in a mixed organic reagent. These prepared NPs were stored at 4 °C.

2.3. *Characterization of PPa nanoassemblies*

The loading rate of PPa was calculated by the following Eqs. (1) and (2):

$$\text{PPa/PCL-PEG}_{2K}\text{NPs}(\%) = M_{\text{PPa}}/(M_{\text{PPa}} + 10\%\text{M}_{\text{PCL-PEG}_{2K}}) \times 100 \quad (1)$$

$$\text{PPa}/\text{PPa-PEG}_{2K}\ \text{NPs}(\%) = (M_{\text{PPa}} + 10\%\ M_{\text{PPa}})/(M_{\text{PPa}} + 10\%\ M_{\text{PPa-PEG}_{2K}}) \times 100 \quad (2)$$

where M_{PPa} is average molecular weight of PPa; $M_{\text{PCL}-\text{PEG}_{2K}}$ is average molecular weight of PCL-PEG$_{2K}$; $M_{\text{PPa}-\text{PEG}_{2K}}$ is average molecular weight of PPa-PEG$_{2K}$.

Diameters and zeta potentials of the prepared NPs were measured by a Malvern Zetasizer (Nano ZS, UK). Morphological investigation was carried out using a transmission electron microscopy (Hitachi, HT7700, Japan). The samples were stained by phosphotungstic acid. In order to verify the stability of PEGylation on the NPs, non-PEGylated PPa NPs, PPa/PCL-PEG$_{2K}$ NPs and PPa/PPa-PEG$_{2K}$ NPs were added dropwise to a phosphate buffer solution (PBS, pH 7.4), and the morphological changes of the NPs were observed. In order to further investigate the stability of the two PEGylated NPs, the changes of the NPs incubated in PBS containing 10% of FBS were determined at each time point in 37 °C. To analyze the effect of laser irradiation on the stability of PPa-nanoassembly, changes in particle size of PPa/PCL-PEG$_{2K}$ NPs or PPa/PPa-PEG$_{2K}$ NPs incubated in PBS (pH 7.4, 37 °C) were investigated under different laser irradiation time (660 nm, 200 mW/cm^2) or without irradiation. The diameters of PPa/PCL-PEG$_{2K}$ NPs or PPa/PPa-PEG$_{2K}$ NPs after laser treatment were measured by a Malvern Zetasizer (Nano ZS).

2.4. *Self-assembly mechanisms*

Exploration of the self-assembly mechanisms of PPa molecules and analysis of intermolecular interactions were performed by computer simulations. Molecular docking calculations were conducted using the Vina protocol in Yinfo Cloud Platform. The 3D structure of PPa was constructed with energy minimization in MMFF94 force field. AutoDock Vina program was utilized to perform semi-flexible docking with maximum nine poses output after internal clustering[33].

To further explore self-assembly mechanisms of PPa-nanoassembly, non-PEGylated PPa NPs, PPa/PCL-PEG$_{2K}$ NPs or PPa/PPa-PEG$_{2K}$ NPs were added to the solutions containing NaCl (50 mmol/L), SDS (50 mmol/L) or urea (50 mmol/L), and were incubated in a shaker in 37 °C. The particle size changes of non-PEGylated PPa NPs, PPa/PCL-PEG$_{2K}$ NPs or PPa/PPa-PEG$_{2K}$ NPs were measured by a Malvern Zetasizer (Nano ZS).

2.5. *Ultraviolet and fluorescence spectra*

The PPa ultraviolet (UV) absorbance spectra of PPa solution (PPa dissolved in DMSO), PPa/PCL-PEG$_{2K}$ NPs or PPa/PPa-PEG$_{2K}$ NPs (1 μmol/L, PPa equivalent) were measured by ultraviolet spectrophotometer (UV1102II, China). The PPa fluorescence spectra of PPa solution, PPa/PCL-PEG$_{2K}$ NPs or PPa/PPa-PEG$_{2K}$ NPs (1 mmol/L, PPa equivalent) were characterized using a microplate reader (Thermo Scientific, USA).

2.6. *In vitro drug release*

The *in vitro* drug release of PPa from the nanoassembly was explored using a common dialysis method. PBS (pH 7.4) containing 20% tetrahydrofuran was used as the release medium. First, a dialysis bag containing 1 mL of PPa solution, PPa/PCL-PEG$_{2K}$ NPs or PPa/PPa-PEG$_{2K}$ NPs were added to 30 mL release medium in a shaker (100 rpm) at 37 °C. PPa solution was prepared by dissolving PPa in a mixed solution of cremophor EL and absolute ethyl alcohol (50/50, *v/v*) and diluted by deionized water as dispersion medium. Then, 1 mL of the release medium was taken out at predetermined timepoints, and was diluted with DMSO and measured using a microplate reader with excitation at 415 nm and emission at 675 nm (Thermo Scientific). Meanwhile, 1 mL of fresh release medium was supplemented to the release medium.

2.7. *In vitro singlet oxygen generation*

The production of singlet oxygen under laser irradiation was detected by SOSG. Briefly, PPa solution, PPa/PCL-PEG$_{2K}$ NPs or PPa/PPa-PEG$_{2K}$ NPs (1 mmol/L, PPa equivalent) mixed with SOSG (1 mmol/L) were diluted in 1 mL of deionized water as dispersion medium. PPa solution was prepared by dissolving PPa in DMSO and diluted by deionized water as dispersion medium. The amount of singlet oxygen generated in these samples was detected under different laser irradiation time (660 nm, 200 mW/cm^2) or without irradiation. The fluorescence signal intensity was measured using a microplate reader with excitation at 504 nm and emission at 525 nm (Thermo Scientific).

2.8. *Cell culture*

Mouse breast cancer 4T1 cells were cultured in Gibco cell culture medium containing 10% FBS, penicillin and streptomycin. After the cells reached 85%, they were digested with trypsin for 3 min, replaced with fresh culture medium, and further cultivated.

2.9. *Cellular uptake and cellular ROS detection*

4T1 cells (1 × 10^5 cells/well) were seeded in 12-well plates and cultured for 24 h. Then, the medium was replaced with PPa solution, PPa/PCL-PEG$_{2K}$ NPs or PPa/PPa-PEG$_{2K}$ NPs and further cultured for 0.5 h or 2 h at 37 °C. PPa solution was prepared by dissolving PPa in DMSO and diluted by fresh cell culture medium. All the formulations contained a total PPa concentration of 50 nmol/L (of which PPa/PPa-PEG$_{2K}$ NPs, free PPa/PPa-PEG$_{2K}$ = 10/1, mol/mol). After incubation, they were washed three times with cold PBS, fixed with 4% cell tissue fixation solution for 15 min, then washed three times with cold PBS, stained with Hoechst for 10 min, and washed three times with cold PBS. Finally, the fluorescence intensity of cells was observed using a laser confocal microscope (Nikon C2, Japan).

For further quantitative analysis, 1 × 10^5 cells were seeded in 12-well plates, and after 24 h of incubation, they were replaced with fresh culture medium containing drugs (PPa solution, PPa/PCL-PEG$_{2K}$ NPs and PPa/PPa-PEG$_{2K}$ NPs) for 0.5 or 2 h. After incubation, the cells were washed, digested, and after being dispersed in PBS. Then, their fluorescence signal intensity was detected by FACSCalibur flow cytometer. Moreover, in order to eliminate the fluorescent interference of aggregation caused quenching (ACQ) effect and to further accurately evaluate the cell uptake efficiency of PPa-nanoassembly, cells incubated with PPa solution or PPa-nanoassembly were digested and collected. Then, the cells were further destroyed by ultrasonic crushing, and methanol was utilized to destroy the nanostructure and dissolve the fluorescent agent (PPa). Finally, the real fluorescent intensity within cells were quantitatively measured using a microplate reader (Thermo Scientific).

4T1 cells were seeded in a 24-well plate at a density of 5 × 10^4 cells per well. After 24 h of incubation, the medium was discarded, and the cells were further placed in a 37 °C cell culture incubator with a fresh medium containing PPa solution, PPa/PCL-PEG$_{2K}$ NPs and PPa/PPa-PEG$_{2K}$ NPs (20 nmol/L, PPa equivalent) and continued to cultivate. After 4 h of incubation, the drug-containing medium was removed, and the serum-free 1640 medium containing DCFH-DA (20 mmol/L) was further incubated for 0.5 h. After the incubation, the cells were irradiated with laser (5 min, 660 nm, 60 mW/cm^2), and the unirradiated cells were used as the control group. Cells were then washed three times with cold PBS, and the fluorescence signal of DCF in the cells was observed using an inverted fluorescence microscopy with an Ex/Em of 488/525 nm. After a similar procedure, the fluorescence intensity was quantified by flow cytometry.

2.10. *Cytotoxicity evaluation*

In order to test the anti-tumor activity of several preparations *in vitro*, 1 × 10^3 cells were seeded in 96-well plates and incubated for 24 h, then replaced with fresh culture medium containing drug (PPa solution, PPa/PCL-PEG$_{2K}$ NPs and PPa/PPa-PEG$_{2K}$ NPs) and incubated for 4 h. After that, the drug-containing medium was washed away with cold PBS and added fresh culture medium or continued the culture without removing the previous drugs, and then irradiated with laser (5 min, 660 nm, 60 mW/cm^2), and continued to incubate for 44 h. Finally, MTT was used to evaluate cell viability.

2.11. *Animal studies*

All experimental procedures were executed according to the protocols approved by Shenyang Pharmaceutical University Animal Care and Use Committee.

2.12. *Pharmacokinetics*

Male Sprague–Dawley rats (200–220 g) were utilized to explore the pharmacokinetics of PPa solution, PPa/PCL-PEG$_{2K}$ NPs and PPa/PPa-PEG$_{2K}$ NPs. PPa solution was prepared by dissolving PPa in a mixed solution of cremophor EL and absolute ethyl alcohol (50/50, *v/v*) and diluted by PBS. The animals were fasted for 12 h before administration. PPa solution, PPa/PCL-PEG$_{2K}$ NPs and

PPa/PPa-PEG_{2K} NPs were respectively injected into the tail vein of rats (1 mg/kg, PPa equivalent) At predetermined intervals, blood samples were collected and immediately centrifuged at 10,000 rpm (Shanghai Anting Scientific Instrument Factory, TGL-16B, Shanghai, China) for 10 min to obtain plasma. Plasma samples were stored at −20 °C for the following analysis. PPa in plasma was extracted by a methanol protein precipitation method. Briefly, 50 μL plasma sample was added to 250 μL methanol and vortexed for 3 min. After vortex, the solution was centrifuged at 5000 rpm (Shanghai Anting Scientific Instrument Factory) for 5 min to obtain free PPa. Then, the concentrations of PPa in various formulations were measured using a microplate reader with excitation at 415 nm and emission at 675 nm (Thermo Scientific).

2.13. *In vivo real-time and ex vivo biodistribution*

A 4T1 tumor-bearing BALB/c mouse model was established by subcutaneously injecting 100 μL of tumor cells (1×10^7 cells/mL) into the right back side of the mice (20−22 g). When the tumor volume reached 300 mm^3, the mice were randomly divided into three groups ($n = 3$). PPa solution, PPa/PCL-PEG_{2K} NPs and PPa/PPa-PEG_{2K} NPs (1 mg/kg, PPa equivalent) were injected intravenously into mice. At predetermined times (2, 4, 6 and 12 h), real-time fluorescent images of the living were taken using the IVIS spectroscopy small animal imaging system. Additionally, for the quantitative analysis of major organs and tumor tissues, a new batch of 4T1 tumor-bearing BABL/c mice were established and treated with the same dose of PPa solution, PPa/PCL-PEG_{2K} NPs and PPa/PPa-PEG_{2K} NPs (1 mg/kg, PPa equivalent). The mice were sacrificed at predetermined time intervals (2, 4, 6 and 12 h) after intravenous injection. The hearts, livers, spleens, lungs, kidneys and tumors were collected and analyzed using the IVIS spectroscopy small animal imaging system. Moreover, high intensity ultrasound was used to destroy the cellular structures of main organs and tumors, and methanol was utilized to destroy the nanostructures of nanoassemblies and to dissolve PPa for the precise quantitative analysis using a microplate reader with excitation at 415 nm and emission at 675 nm (Thermo Scientific).

2.14. *In vivo antitumor activity*

The BALB/c mice bearing 4T1 xenograft tumors were used for the evaluation of antitumor *in vivo*. When the tumor volume grew to about 150 mm^3, the established tumor-bearing mice were randomly divided into 4 groups ($n = 5$). PPa solution, PPa/PCL-PEG_{2K} NPs or PPa/PPa-PEG_{2K} NPs were injected *via* the tail vein of mice at a dose of 4 mg/kg (PPa equivalent) and taken once every other day. After 4 h of administration, the set light group was given a laser (5 min, 660 nm, 200 mW/cm^2). The non-light group was placed in a dark place to avoid being activated. Tumor volumes and body weights of mice were measured and recorded daily.

After the *in vivo* anti-tumor experiment was completed, blood was collected from the tumor-bearing mice. The collected blood was centrifuged to take the upper serum and sent to the blood analysis center to measure liver and kidney function indicators. The main indicators included: alanine aminotransferase (ALT), aspartate aminotransferase (AST), blood urine nitrogen (BUN) and creatinine (CRE).

After the tumor-bearing mice were sacrificed, mice were dissected to obtain the main organs and tumors. After being washed three times with PBS, 4% paraformaldehyde solution was used to treat the organ and tumor tissues. Then, the samples were sent to the center of tissue section, embedded in paraffin, frozen section, and finally stained. The sections were observed using an inverted biological microscopy (Nikon, Japan).

2.15. *Statistical analysis*

All the data were displayed as mean value ± standard deviation. Student's *t*-test and one-way analysis of variance were applied to statistical difference, and $P < 0.05$ was regarded as significant difference.

3. Results and discussion

3.1. *Self-assembly of PPa*

Although a variety of PPa-encapsulated nano-DDS have been widely investigated for PDT, the self-assembly capacity of PPa hasn't been found yet. In the present study, we found that pure PPa could self-assemble into NPs by using a facile nano-precipitation method. When PPa dissolved in a mixed solution of tetrahydrofuran and ethanol was added dropwise to water, nanoassembly occurred spontaneously even without the help of any surfactant (Supporting Information Fig. S1). Tetrahydrofuran and ethanol were removed by a vacuum rotary evaporator at room temperature. The particle size of PPa-nanoassembly was about 100 nm, with a zeta potential of around −20 mV (Fig. 2B and Supporting Information Table S1). By contrast, PPa powder couldn't be dissolved in water and precipitated immediately due to its poor water solubility (Supporting Information Fig. S1).

In order to further strengthen the nanostructure of PPa-nanoassembly, an amphiphilic polymeric PEG_{2K}-PPa was synthesized according to our previous method[31]. PEG_{2K}-PPa was utilized to prepare a uniquely core-matched nanostructure (PPa/PPa-PEG_{2K} NPs). Another amphiphilic polymer PCL-PEG_{2K} with similar molecular weight was used as control. Finally, PPa-PEG_{2K} (10%, mol/mol) and PCL-PEG_{2K} (10%, mol/mol) were used to form a hydrophilic shell in the fabrication of PPa/PPa-PEG_{2K} NPs and PPa/PCL-PEG_{2K} NPs, respectively. As shown in Fig. 2B and Supporting Information Table S1, the drug loading rates of PPa in PPa/PPa-PEG_2K NPs and PPa/PCL-PEG_{2K} NPs were 74.8% and 68.3%, respectively. The slightly higher drug loading capacity of PPa/PPa-PEG_{2K} NPs should be attributed to the contribution of the PPa in PPa-PEG_{2K} polymer.

The self-assembly mechanisms of PPa were explored through molecular docking simulation. As shown in Fig. 2A, PPa molecules could form nano-aggregates in a stable thermodynamic state. Notably, the multiple pyrrole hybrid structures of PPa endowed strong π–π stacking effect and hydrophobic force among PPa molecules, which made a significant contribution to the formation of self-assembled NPs (Fig. 2A). Additionally, as shown in Fig. 2C and Supporting Information Fig. S4, obvious red shift was observed in the UV absorbance spectra and fluorescence spectrum of non-PEGylated PPa NPs, PPa/PPa-PEG_{2K} NPs and PPa/PCL-PEG_{2K} NPs when compared with PPa solution. However, the fluorescence intensity of PPa-nanoassembly decreased when compared with PPa solution, due to the ACQ effect and the exciton migration during π–π stacking interaction between PPa molecules and the molecular conformation change in process of assembly[23,34,35]. Notably, when compared with non-PEGylated PPa NPs, the fluorescence intensity of PPa/PCL-PEG_{2K} NPs further decreased, but no fluorescent reduce was observed in

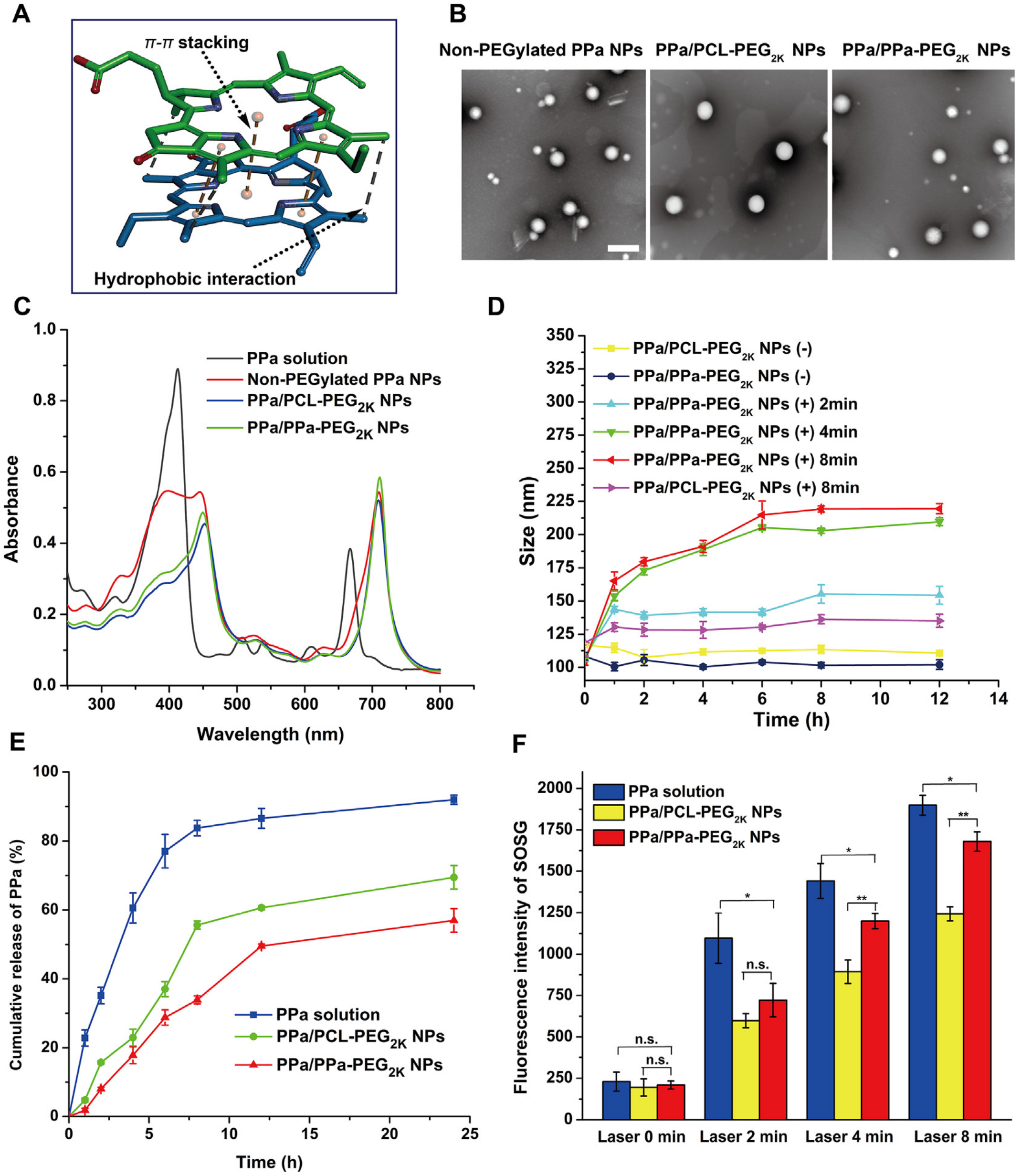

Figure 2 Self-assembly of PPa and *in vitro* singlet oxygen production efficiency of formulations. (A) Self-assembly simulation of PPa in water. (B) TEM images of non-PEGylated PPa NPs, PPa/PCL-PEG$_{2K}$ NPs and PPa/PPa-PEG$_{2K}$ NPs (scale bar represents 200 nm). (C) UV absorption spectra at 250−800 nm wavelength of PPa solution, non-PEGylated PPa NPs, PPa/PCL-PEG$_{2K}$ NPs and PPa/PPa-PEG$_{2K}$ NPs. (D) Changes in particle size of PPa/PCL-PEG$_{2K}$ NPs and PPa/PPa-PEG$_{2K}$ NPs with different laser time. (E) *In vitro* accumulative drug release curves of PPa from PPa solution, PPa/PCL-PEG$_{2K}$ NPs and PPa/PPa-PEG$_{2K}$ NPs in PBS containing 20% tetrahydrofuran within 24 h. (F) Fluorescence intensity of singlet oxygen produced by formulations *in vitro* (parameters of microplate reader: excitation at 415 nm and emission at 675 nm). Data are shown as the mean ± SD, $n = 3$; $^{*}P < 0.05$, $^{**}P < 0.01$.

PPa/PPa-PEG$_{2K}$ NPs group. These results indicated that PPa/PPa-PEG$_{2K}$ NPs showed advantages in relieving the ACQ effect.

To further explore the self-assembly mechanisms of PPa-nanoassembly, SDS, urea and NaCl were utilized to verify the existence of hydrophobic interaction, hydrogen-bond interaction and electrostatic interaction in the PPa-nanoassembly. As shown in Supporting Information Fig. S5, non-PEGylated PPa NPs, PPa/PCL-PEG$_{2K}$ NPs and PPa/PPa-PEG$_{2K}$ NPs showed no significant change in particle size after incubation with urea, but their particle size obviously increased after incubation with SDS. Notably, the particle size of non-PEGylated PPa NPs treated with sodium chloride significantly increased when compared with PPa/PCL-PEG$_{2K}$ NPs and PPa/PPa-PEG$_{2K}$ NPs. These results demonstrated that multiple interactions and forces were involved in the self-assembly process of PPa. Moreover, PEGylation modification significantly improved the colloidal stability of PPa-nanoassembly.

3.2. *Stability of PPa-nanoassembly*

The colloidal stability of NPs is extremely important for efficient drug delivery. As shown in Supporting Information Fig. S2, the non-PEGylated PPa NPs quickly precipitated in PBS due to the salting-out effect. In contrast, PPa/PCL-PEG$_{2K}$ NPs and PPa/PPa-PEG$_{2K}$ NPs could remain good colloidal stability in PBS even for one week. Notably, PPa/PPa-PEG$_{2K}$ NPs showed much better colloidal stability in PBS containing 10% FBS than PPa/PCL-PEG$_{2K}$ NPs (Supporting Information Fig. S3). The excellent colloidal stability of PPa/PPa-PEG$_{2K}$ NPs should be attributed to the core-matched stabilizing effect of PPa-PEG$_{2K}$, which could form a more stable core-shell nanostructure due to the π–π stacking effect and hydrophobic interaction between the PPa core and the PPa-PEG$_{2K}$ shell. These results suggest that core-matched PEGylating modification could be utilized as an efficient strategy to significantly increase the colloidal stability of pure drug-driven nanoassembly. Which would benefit the efficient drug delivery of PPa-nanoassembly *in vivo*.

We then investigated the impact of laser irradiation on the colloidal stability of PPa-nanoassembly by determining the changes in particle size changes with/without laser irradiation. As shown in Fig. 2D, the particle size of PPa/PPa-PEG$_{2K}$ NPs significantly increased within 4 min under laser irradiation. By contrast, there was almost no significant increase in the particle size of PPa/PCL-PEG$_{2K}$ NPs exposed to the laser even for a longer irradiation time (8 min). Obviously, PEGylation modification on PPa-nanoassembly could significantly increase the colloidal stability. But only PPa/PPa-PEG$_{2K}$ NPs showed laser-triggered disassembly phenomenon, owing to the photobleaching of the PPa fraction in PPa-PEG$_{2K}$ polymer under laser irradiation. As a result, the amphipathic structure of PPa-PEG$_{2K}$ polymer was broken, resulting in the decrease of PEGylation stabilization on PPa-nanoassembly. In contrast, laser exerted marginal influence on PCL-PEG$_{2K}$. As a result, PCL-PEG$_{2K}$ could maintain the good stability of PPa/PCL-PEG$_{2K}$ NPs with or without laser treatment. The slight change ($\sim$30 nm) in particle size of PPa/PCL-PEG$_{2K}$ NPs exposed to laser treatment should be contributed to the gradual photobleaching effects on the PPa core. These results illustrate that core-matched PPa/PPa-PEG$_{2K}$ NPs could not only significantly improve the colloidal stability of PPa-nanoassembly, but also demonstrated laser-triggered destabilization of the nanoassembly. Such a laser-triggered destabilization is expected to facilitate its photoconversion and ROS generation efficiency.

3.3. *In vitro drug release*

As shown in Fig. 2E, the release rate of PPa from PPa solution was much faster than that from both PPa/PCL-PEG$_{2K}$ NPs and PPa/PPa-PEG$_{2K}$ NPs. More than 60% of PPa was released from PPa solution within 4 h, while only about 20% of PPa was released from PPa/PCL-PEG$_{2K}$ NPs and PPa/PPa-PEG$_{2K}$ NPs under the same conditions. These results indicate that PPa solution showed an initial burst release phenomenon, but PPa/PCL-PEG$_{2K}$ NPs and PPa/PPa-PEG$_{2K}$ NPs revealed sustained drug release features.

3.4. *In vitro singlet oxygen generation*

The *in vitro* singlet oxygen generation efficiencies of PPa solution, PPa/PCL-PEG$_{2K}$ NPs and PPa/PPa-PEG$_{2K}$ NPs were investigated using SOSG. PPa solution was prepared by dissolving PPa in DMSO and diluted by deionized water. As shown in Fig. 2F, the amount of singlet oxygen produced by the three formulations was extremely low without laser irradiation, but the fluorescence intensity of SOSG significantly increased in an irradiation time-dependent manner. Under laser irradiation, the amount of singlet oxygen produced by PPa solution was somewhat higher than that of PPa/PCL-PEG$_{2K}$ NPs and PPa/PPa-PEG$_{2K}$ NPs. Which should be attributed to the aggregation-caused reduction of photo-induced ROS generation in PPa-nanoassembly. Notably, although there was no significant difference in the fluorescence intensity of PPa/PCL-PEG$_{2K}$ NPs and PPa/PPa-PEG$_{2K}$ NPs exposed to the laser within 2 min, the amount of singlet oxygen produced from PPa/PPa-PEG$_{2K}$ NPs was much more than that from PPa/PCL-PEG$_{2K}$ NPs with the laser exposure time extended to 4 or 8 min. These results reveal that short time laser treatment triggered the rapid increase of particle size and the formation of the fluffy state of PPa/PPa-PEG$_{2K}$ NPs, significantly relieving the aggregation-caused reduction of photo-induced ROS generation (Fig. 2D and F). As a result, singlet oxygen generation from PPa/PPa-PEG$_{2K}$ NPs was much higher than that from PPa/PCL-PEG$_{2K}$ NPs when exposed to a longer laser irradiation time. Moreover, when compared with non-PEGylated PPa NPs, the fluorescence intensity of PPa/PCL-PEG$_{2K}$ NPs decreased, but there's no fluorescent reduce observed in PPa/PPa-PEG$_{2K}$ NPs group (Supporting Information Fig. S4). These results indicate that PPa/PPa-PEG$_{2K}$ NPs showed advantages in relieving the aggregation-caused reduction of photo-induced ROS generation and ACQ effect of fluorescence. These results are in well consistence with the fluorescence spectra and the colloidal stability results (Fig. 2D and Supporting Information Fig. S4).

3.5. *Cellular uptake and intracellular ROS generation*

The inherent fluorescence of PPa makes it convenient to monitor the cellular uptake of the nanoassembly. Moreover, the fluorescence spectra of PPa-PEG$_{2K}$ had no significant change compared with PPa[31], making it convenient to accurately calculate the molar dose of PPa. The cellular uptake was explored using 4T1 breast cancer cells treated with PPa solution, PPa/PCL-PEG$_{2K}$ NPs and PPa/PPa-PEG$_{2K}$ NPs (50 nmol/L, PPa equivalent), As shown in Fig. 3A–D and Supporting Information Fig. S6, the cellular uptake of all formulations demonstrated a time-dependent manner, but PPa/PCL-PEG$_{2K}$ NPs and PPa/PPa-PEG$_{2K}$ NPs showed much higher cellular uptake efficiency than PPa solution at both 0.5 and 2 h. In addition, there's no obvious difference in the fluorescence intensity between PPa/PCL-PEG$_{2K}$ NPs and PPa/PPa-PEG$_{2K}$ NPs, due to their very similar nanostructures. These results suggest that PPa-nanoassembly could significantly improve the cellular internalization of PPa, probably due to nanoparticle-mediated endocytosis[36,37].

We further detected the intracellular ROS generation capacity of PPa-nanoassembly. An ROS probe (2′,7′-dichlorofluorescein diacetate, DCFH-DA) can be hydrolyzed by the intracellular esterase to generate DCFH, and the fluorescent DCF could be generated after the oxidization of DCFH by ROS. The fluorescence intensity of DCF was utilized for intracellular ROS detection. As shown in Fig. 4A and B, the fluorescence intensity of PPa/PPa-PEG$_{2K}$ NPs and PPa/PCL-PEG$_{2K}$ NPs were significantly higher than that of PPa solution, owing to the higher cellular uptake of PPa-nanoassembly. Notably, despite of their similar cellular uptake efficiency, PPa/PPa-PEG$_{2K}$ NPs exhibited higher intracellular ROS generation capacity than that of PPa/PCL-PEG$_{2K}$ NPs, which should be attributed to the relieved aggregation-caused reduction of ROS generation in PPa/PPa-PEG$_{2K}$ NPs under laser irradiation.

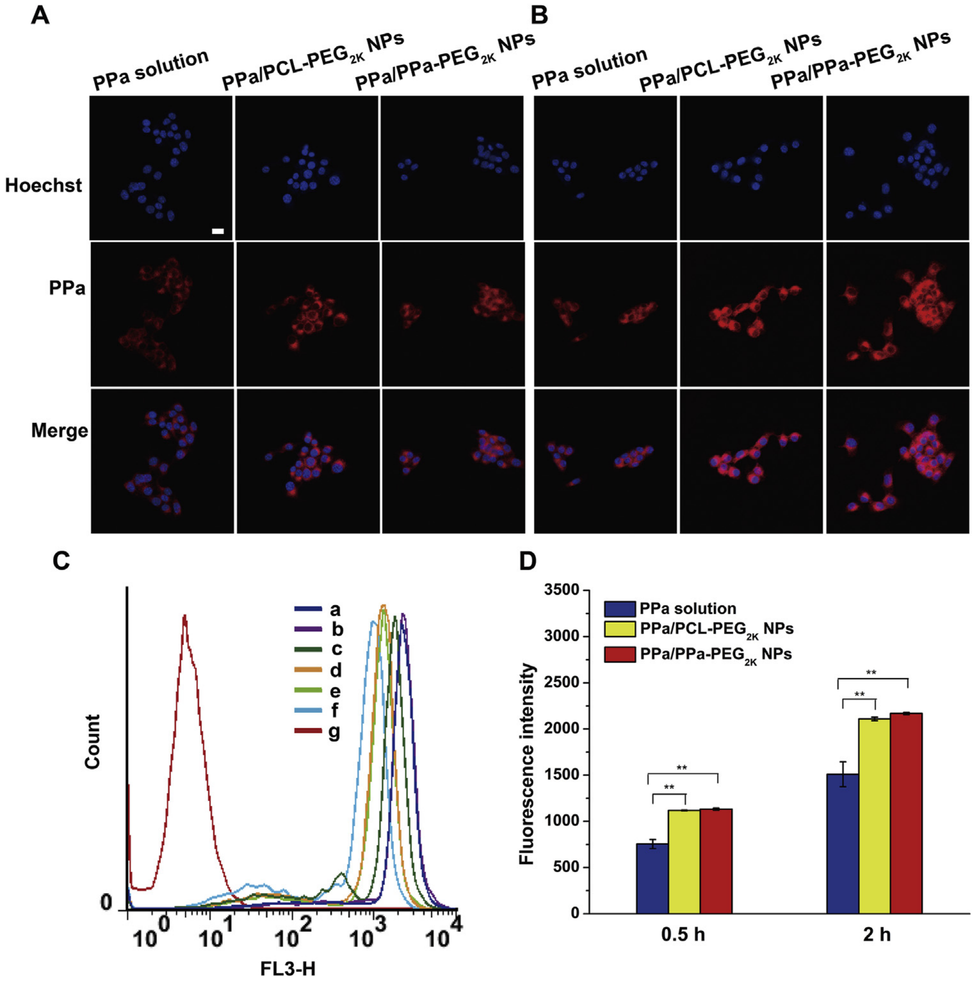

Figure 3 Cellular uptake of PPa solution, PPa/PCL-PEG$_{2K}$ NPs and PPa/PPa-PEG$_{2K}$ NPs. (A) Confocal laser scanning microscopy (CLSM) images at 0.5 h or (B) 2 h. (C) Flow analysis diagram by flow cytometry (a: PPa/PPa-PEG$_{2K}$ NPs 2 h, b: PPa/PCL-PEG$_{2K}$ NPs 2 h, c: PPa solution 2 h, d: PPa/PPa-PEG$_{2K}$ NPs 0.5 h, e: PPa/PCL-PEG$_{2K}$ NPs 0.5 h, f: PPa solution 0.5 h, g: Blank). (D) Quantitative analysis for the fluorescent intensity by flow cytometry. Data are shown as the mean ± SD, $n = 3$; $^*P < 0.05$, $^{**}P < 0.01$. Scale bar = 10 μm.

3.6. *Cytotoxicity*

Higher cellular uptake efficiency of PPa/PCL-PEG$_{2K}$ NPs and PPa/PPa-PEG$_{2K}$ NPs might result in more potent cytotoxicity. Distinguished from other cytotoxic drugs, the cytotoxicity of PSs depends on the generation of ROS under laser irradiation. Notably, both the extracellular and intracellular PSs could produce ROS and damage the structures and functions of cells under laser treatment. As shown in Fig. 4C and Supporting Information Table S2, there's no significant difference in the cytotoxicity of PPa solution, PPa/PCL-PEG$_{2K}$ NPs and PPa/PPa-PEG$_{2K}$ NPs without removing the drug-containing culture medium before laser irradiation. By contrast, PPa/PCL-PEG$_{2K}$ NPs and PPa/PPa-PEG$_{2K}$ NPs showed more potent cytotoxicity against 4T1 cells than PPa solution when the drug-containing cell culture medium was replaced by fresh medium before laser irradiation (Fig. 4D and Supporting Information Table S2). Moreover, PPa/PPa-PEG$_{2K}$ NPs had a higher cytotoxicity than PPa/PCL-PEG$_{2K}$ NPs, which should be attributed to the higher ROS generation capacity of PPa/PPa-PEG$_{2K}$ NPs (Fig. 4A and B). As expected, all the three formulations showed negligible cytotoxicity without laser irradiation. These results suggested that both the extracellular and intracellular PPa contributed to the ROS-induced cytotoxicity against tumor cells. When the drug-containing cell culture medium was replaced by fresh medium before laser irradiation, the cellular uptake efficiency and ROS production capacity of PPa-nanoassembly exerted obvious impact on the cytotoxicity. As a result, PPa/PPa-PEG$_{2K}$ NPs, with good colloidal stability, favorable cellular uptake and efficient ROS production, showed more potent phototoxicity against 4T1 cells than PPa/PCL-PEG$_{2K}$ NPs and PPa solution.

3.7. *Pharmacokinetics*

The pharmacokinetic profiles of PPa solution, PPa/PPa-PEG$_{2K}$ NPs and PPa/PCL-PEG$_{2K}$ NPs were investigated in rats. The concentration–time curves and pharmacokinetics parameters were shown and summarized in Fig. 5 and Supporting Information Table S3, respectively. As expected, PPa/PPa-PEG$_{2K}$ NPs and PPa/PCL-PEG$_{2K}$ NPs significantly prolonged the systemic circulation time of PPa when compared with PPa solution. Notably,

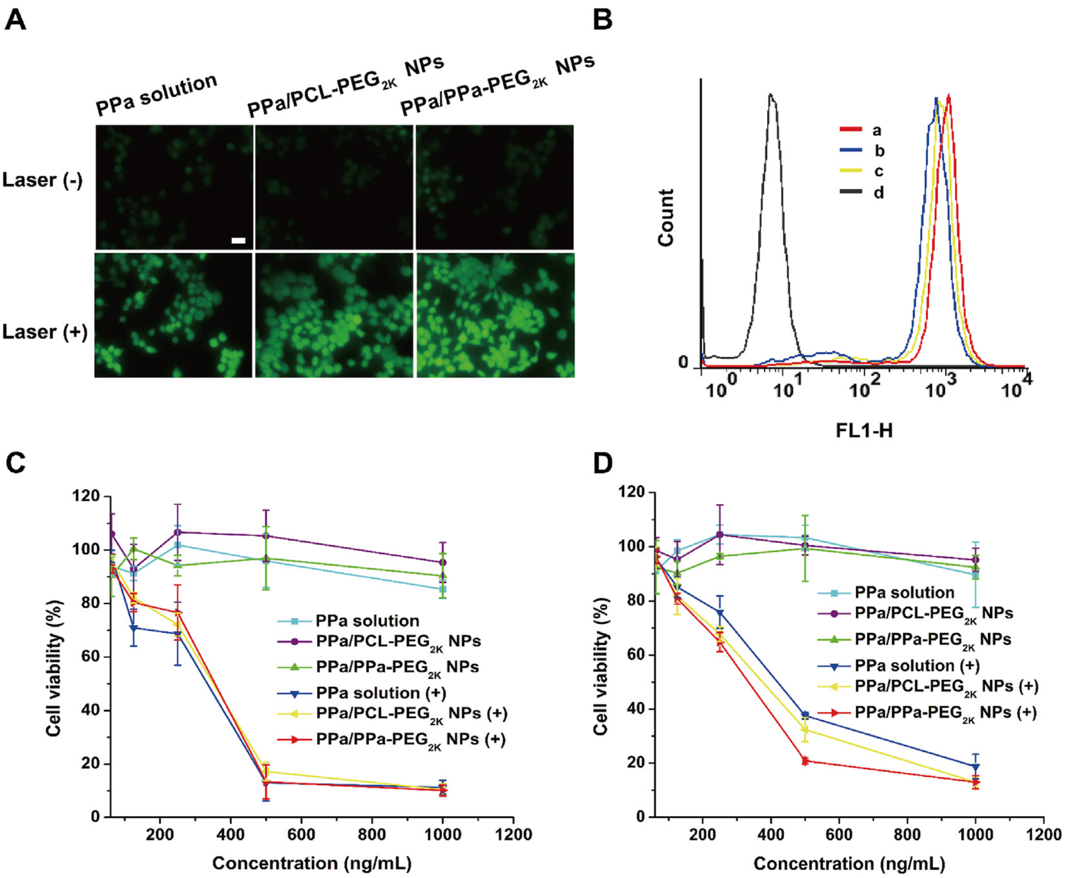

Figure 4 *In vitro* cellular ROS production efficiency and photodynamic cytotoxicity. (A) Fluorescence image of ROS produced in cells with PPa solution, PPa/PCL-PEG$_{2K}$ NPs and PPa/PPa-PEG$_{2K}$ NPs using inverted fluorescence microscope. (B) Quantitative analysis of fluorescence intensity using flow cytometry (a: PPa solution (+); b: PPa/PCL-PEG$_{2K}$ NPs (+); c: PPa/PPa-PEG$_{2K}$ NPs (+), d: Blank). (C) Cell viability treated with PPa solution, PPa/PCL-PEG$_{2K}$ NPs and PPa/PPa-PEG$_{2K}$ NPs. (D) Cell viability with removing the drug-containing culture medium before laser irradiation. Data are shown as the mean ± SD, $n = 3$. Scale bar = 10 μm.

PPa/PPa-PEG$_{2K}$ NPs exhibited longer circulation time in blood than PPa/PCL-PEG$_{2K}$ NPs, which should be attributed to the core-matched PEGylating stabilization of PPa-PEG$_{2K}$. These results illustrate that PEGylating modification could be of benefit to the *in vivo* drug delivery efficiency of PPa-nanoassembly. More importantly, such a core-matched PEGylated strategy could further extend the systemic circulation of PPa, thus facilitating preferable drug accumulation in tumors *via* the enhanced permeability and retention (EPR) effect[38].

3.8. *In vivo imaging and ex vivo biodistribution*

As PPa is a near-infrared dye, its nanoassembly is inherently equipped with self-tracking capacity for imaging-guided drug delivery. The *in vivo* real-time imaging of PPa-nanoassembly was investigated in 4T1 tumor-bearing mice. As shown in Supporting Information Fig. S7, PPa solution was quickly cleared from the body with little tumor accumulation. By contrast, PPa/PCL-PEG$_{2K}$ NPs and PPa/PPa-PEG$_{2K}$ NPs exhibited stronger fluorescence intensity in tumors than PPa solution. As expected, the highest fluorescence in tumor was observed at 4 h in mice treated with PPa/PPa-PEG$_{2K}$ NPs due to the better stability and longer circulation time in blood. Moreover, in order to more visually observe the fluorescence intensity of specific organs and tumors, the *ex vivo* biodistribution of PPa solution, PPa/PCL-PEG$_{2K}$ NPs and PPa/PPa-PEG$_{2K}$ NPs was also explored in 4T1 tumor-bearing mice. As shown in Fig. 6A and B, and Supporting Information

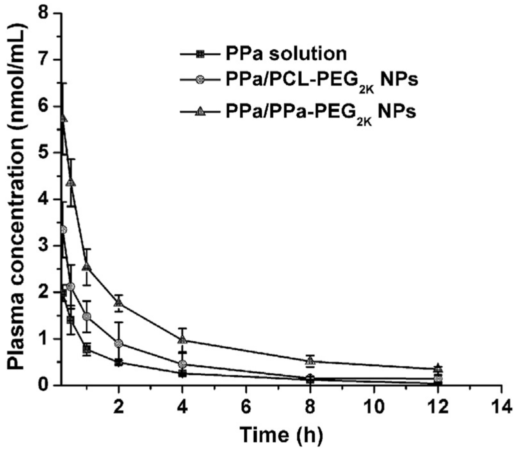

Figure 5 Pharmacokinetics. Plasma concentration-time profiles of PPa solution, PPa/PCL-PEG$_{2K}$ NPs and PPa/PPa-PEG$_{2K}$ NPs after a single intravenous administration. Data are shown as the mean ± SD, $n = 5$.

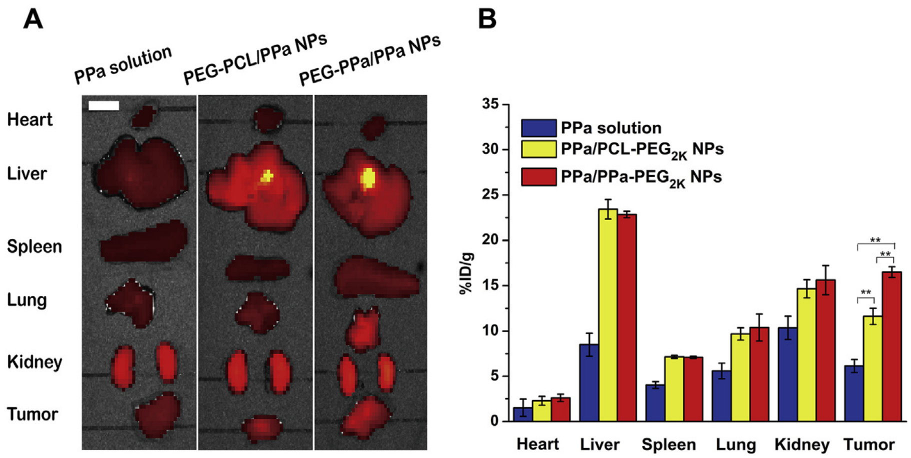

Figure 6 *Ex vivo* biodistribution. (A) *Ex vivo* fluorescent distribution images of PPa in rats after injection with various formulation at 4 h. (B) Quantitative analysis of the percent injected dose. Data are shown as the mean ± SD, $n = 3$; $^{*}P < 0.05$, $^{**}P < 0.01$. Scale bar = 50 mm.

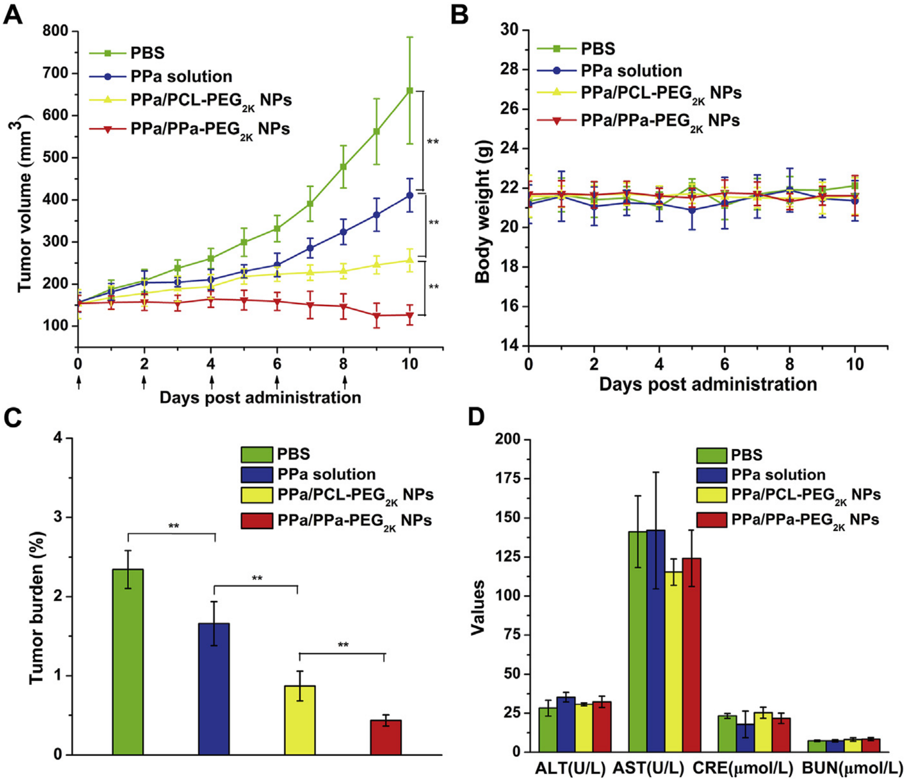

Figure 7 Evaluation on the *in vivo* antitumor activity in BALB/c mice bearing 4T1 tumors. (A) Changes of the tumor volume after PPa solution, PPa/PCL-PEG$_{2K}$ NPs and PPa/PPa-PEG$_{2K}$ NPs treatments. (B) Changes in body weight of mice during treatment. (C) Tumor burden (tumor weight/average body weight) after the last treatment. (D) Liver and kidney functional parameters after the last treatment. Data are shown as the mean ± SD, $n = 5$; $^{*}P < 0.05$, $^{**}P < 0.01$.

Figs. S8 and S9, the *ex vivo* biodistribution is consistent with the result of *in vivo* imaging. Therefore, the optimal laser irradiation time for *in vivo* antitumor activity assay should be 4 h after intravenous injection.

3.9. *In vivo antitumor activity*

Multiple drug delivery advantages make PPa/PPa-PEG$_{2K}$ NPs as a promising nanomedicine for antitumor treatment. The antitumor activity of PPa solution, PPa/PCL-PEG$_{2K}$ NPs and PPa/PPa-PEG$_{2K}$ NPs was evaluated in BALB/c mice bearing 4T1 tumor. When the tumor volume grew to about 150 mm^3, PBS, PPa solution, PPa/PCL-PEG$_{2K}$ NPs and PPa/PPa-PEG$_{2K}$ NPs (2 mg/kg, PPa equivalent) were intravenously administrated once every other day for five injections, respectively. According to the *in vivo* and *ex vivo* biodistribution results, the laser treated groups received a tumor-localized light exposure (200 mW/cm^2) for 5 min at 4 h post administration. As shown in Fig. 7A, C and Supporting Information Fig. S10, PPa solution showed a moderate inhibitory effect on tumor growth when compared with PBS. PPa/PCL-

PEG_{2K} NPs showed a better inhibition effect on tumor growth than that of PPa solution. Notably, PPa/PPa-PEG_{2K} NPs exhibited much more potent anti-tumor activity than both PPa/PCL-PEG_{2K} NPs and PPa solution, which could be attributed to multiply advantages of PPa/PPa-PEG_{2K} NPs: (i) stable nanostructure by virtue of core-matched PEGylating stabilization; (ii) long systemic circulation and high tumor accumulation, (iii) efficient cellular uptake; and (iv) abundant generation of ROS under laser irradiation.

Moreover, there was no significant change in body weights of mice in each group throughout the treatment period (Fig. 7B). Moreover, there was no significant change found in the liver and kidney function parameters based on the serum analysis results (Fig. 7D). In the histological analysis of H&E section staining, there was no significant damage found in the sections of the main organs of each group (Supporting Information Fig. S11). In tumor tissue sections, the largest apoptosis and necrosis spread area was observed in the PPa/PPa-PEG_{2K} NPs group. Therefore, PPa/PPa-PEG_{2K} NPs hold great potential to be used as a promising nanoplatform with high efficiency and low toxicity.

4. Conclusions

In the present study, we reported a unique self-assembly phenomenon of PPa. To enhance the stability of PPa-nanoassembly, core-matched PEGylating modification was developed using a photodynamic PEG polymer (PPa-PEG_{2K}) in the nanoformulation. The core-matched PEGylated nanoassembly (PPa/PPa-PEG_{2K} NPs), with high drug loading capacity and colloidal stability, demonstrated long circulation time in blood, high tumor accumulation, efficient cellular uptake and potent cytotoxicity. As expected, PPa/PPa-PEG_{2K} NPs performed much more potent antitumor activity in 4T1 tumor-bearing BALB/c mice than PPa/PCL-PEG_{2K} NPs and PPa solution. This novel nanosystem could be utilized as a promising nanomedicine for high-efficient imaging-guided cancer therapy by integrating pure drug self-assembly technique and core-matched PEGylation stabilization into one platform.

Acknowledgments

This work was supported by Science and Technology Major Project of Liaoning (No. 2019JH1/10300004, China), the National Natural Science Foundation of China (No. 81773656 and 81703451), the Excellent Youth Science Foundation of Liaoning Province (No. 2020-YQ-06, China), the China Postdoctoral Science Foundation (No. 2020M670794) and the Liaoning Revitalization Talents Program (No. XLYC1907129 and XLYC1808017, China).

Author contributions

Shenwu Zhang, Cong Luo, Jin Sun and Zhonggui He conceived the work. Shenwu Zhang, Yuequan Wang, Zhiqiang Kong participated in the design and implementation of the experiment. Shenwu Zhang, Xuanbo Zhang, Bingjun Sun, Han Yu and Qin Chen carried out data processing and analysis. Shenwu Zhang and Cong Luo wrote and modified paper. All authors discussed and approved the manuscript.

Conflicts of interest

There are no conflicts to declare.

Appendix A. Supporting Information

Supporting data to this article can be found online at https://doi.org/10.1016/j.apsb.2021.04.005.

References

1. Siegel RL, Miller KD, Jemal A. Cancer statistics, 2019. *CA Cancer J Clin* 2019;**69**:7−34.
2. He H, Liu L, Morin EE, Liu M, Schwendeman A. Survey of clinical translation of cancer nanomedicines—lessons learned from successes and failures. *Accounts Chem Res* 2019;**52**:2445−61.
3. Mei D, Chen B, He B, Liu H, Lin Z, Lin J, et al. Actively priming autophagic cell death with novel transferrin receptor-targeted nanomedicine for synergistic chemotherapy against breast cancer. *Acta Pharm Sin B* 2019;**9**:1061−77.
4. Liu A, Wang H, Hou X, Ma Y, Yang G, Hou Y, et al. Combinatory antitumor therapy by cascade targeting of a single drug. *Acta Pharm Sin B* 2020;**10**:667−79.
5. Feliu J, Heredia-Soto V, Gironés R, Jiménez-Munarriz B, Saldaña J, Guillén-Ponce C, et al. Management of the toxicity of chemotherapy and targeted therapies in elderly cancer patients. *Clin Transl Oncol* 2020;**22**:457−67.
6. Deng K, Li C, Huang S, Xing B, Jin D, Zeng Q, et al. Recent progress in near infrared light triggered photodynamic therapy. *Small* 2017;**13**:1702299.
7. Azarabadi S, Abdollahi H, Torabi M, Salehi Z, Nasiri J. ROS generation, oxidative burst and dynamic expression profiles of ROS-scavenging enzymes of superoxide dismutase (SOD), catalase (CAT) and ascorbate peroxidase (APX) in response to Erwinia amylovora in pear (Pyrus communis L). *Eur J Plant Pathol* 2017;**147**:279−94.
8. Luo GF, Chen WH, Hong S, Cheng Q, Qiu WX, Zhang XZ. A Self-transformable pH-driven membrane-anchoring photosensitizer for effective photodynamic therapy to inhibit tumor growth and metastasis. *Adv Funct Mater* 2017;**27**:1702122.
9. Zhang C, Gao F, Wu W, Qiu WX, Zhang L, Li R, et al. Enzyme-driven membrane-targeted chimeric peptide for enhanced tumor photodynamic immunotherapy. *ACS Nano* 2019;**13**:11249−62.
10. Trachootham D, Alexandre J, Huang P. Targeting cancer cells by ROS-mediated mechanisms: a radical therapeutic approach. *Nat Rev Drug Discov* 2009;**8**:579.
11. Zhang C, Chen WH, Liu LH, Qiu WX, Yu WY, Zhang XZ. An O_2 Self-supplementing and reactive-oxygen-species-circulating amplified nanoplatform *via* H_2O/H_2O_2 splitting for tumor imaging and photodynamic therapy. *Adv Funct Mater* 2017;**27**:1700626.
12. Chen MH, Jenh YJ, Wu SK, Chen YS, Hanagata N, Lin FH. Non-invasive photodynamic therapy in brain cancer by use of Tb^{3+}-doped LaF_3 nanoparticles in combination with photosensitizer through X-ray irradiation: a proof-of-concept study. *Nanoscale Res Lett* 2017;**12**:62.
13. Luby BM, Walsh CD, Zheng G. Advanced photosensitizer activation strategies for smarter photodynamic therapy beacons. *Angew Chem Int Ed* 2019;**58**:2558−69.
14. Liu B, Li C, Cheng Z, Hou Z, Huang S, Lin J. Functional nanomaterials for near-infrared-triggered cancer therapy. *Biomater Sci* 2016;**4**:890−909.
15. Zhang W, Wan F, Hu C, Zhou Y, Gao H, Hu J. The progress and perspective of nanoparticle-enabled tumor metastasis treatment. *Acta Pharm Sin B* 2020;**10**:2037−53.
16. Luo Z, Dai Y, Gao H. Development and application of hyaluronic acid in tumor targeting drug delivery. *Acta Pharm Sin B* 2019;**9**:1099−112.
17. Li C, Wang J, Wang Y, Gao H, Wei G, Huang Y, et al. Recent progress in drug delivery. *Acta Pharm Sin B* 2019;**9**:1145−62.

18. Bi D, Zhao L, Yu R, Li H, Guo Y, Wang X, et al. Surface modification of doxorubicin-loaded nanoparticles based on polydopamine with pH-sensitive property for tumor targeting therapy. *Drug Deliv* 2018;**25**: 564−75.
19. Wang J, Pan W, Wang Y, Lei W, Feng B, Du C, et al. Enhanced efficacy of curcumin with phosphatidylserine-decorated nanoparticles in the treatment of hepatic fibrosis. *Drug Deliv* 2018;**25**:1−11.
20. Li S, Shan X, Wang Y, Chen Q, Sun J, He Z, et al. Dimeric prodrug-based nanomedicines for cancer therapy. *J Control Release* 2020;**326**: 510−22.
21. Yang F, Zhao Z, Sun B, Chen Q, Sun J, He Z, et al. Nanotherapeutics for antimetastatic treatment. *Trends Cancer* 2020;**6**:645−59.
22. Debele T, Peng S, Tsai HC. Drug carrier for photodynamic cancer therapy. *Int J Mol Sci* 2015;**16**:22094−136.
23. Jia Q, Ge J, Liu W, Guo L, Zheng X, Chen S, et al. Self-assembled carbon dot nanosphere: a robust, near-infrared light-responsive, and vein injectable photosensitizer. *Adv Healthc Mater* 2017;**6**:1601419.
24. Zheng X, Ge J, Wu J, Liu W, Guo L, Jia Q, et al. Biodegradable hypocrellin derivative nanovesicle as a near-infrared light-driven theranostic for dually photoactive cancer imaging and therapy. *Biomaterials* 2018;**185**:133−41.
25. Guan M, Ge J, Wu J, Zhang G, Chen D, Zhang W, et al. Fullerene/photosensitizer nanovesicles as highly efficient and clearable phototheranostics with enhanced tumor accumulation for cancer therapy. *Biomaterials* 2016;**103**:75−85.
26. Lv S, Wu Y, Cai K, He H, Li Y, Lan M, et al. High drug loading and sub-quantitative loading efficiency of polymeric micelles driven by donor−receptor coordination interactions. *J Am Chem Soc* 2018;**140**: 1235−8.
27. Wen Y, Zhang W, Gong N, Wang YF, Guo HB, Guo W, et al. Carrier-free, self-assembled pure drug nanorods composed of 10-hydroxycamptothecin and chlorin e6 for combinatorial chemo-photodynamic antitumor therapy *in vivo*. *Nanoscale* 2017;**9**:14347−56.
28. Zhang X, Sun B, Zuo S, Chen Q, Gao Y, Zhao H, et al. Self-assembly of a pure photosensitizer as a versatile theragnostic nanoplatform for imaging-guided antitumor photothermal therapy. *ACS Appl Mater Interfaces* 2018;**10**:30155−62.
29. Fan L, Zhang B, Xu A, Shen Z, Guo Y, Zhao R, et al. Carrier-free, pure nanodrug formed by the self-assembly of an anticancer drug for cancer immune therapy. *Mol Pharmaceut* 2018;**15**: 2466−78.
30. Zhang X, Li N, Zhang S, Sun B, Chen Q, He Z, et al. Emerging carrier-free nanosystems based on molecular self-assembly of pure drugs for cancer therapy. *Med Res Rev* 2020;**40**:1754−75.
31. Sun B, Chen Y, Yu H, Wang C, Zhang X, Zhao H, et al. Photodynamic PEG-coated ROS-sensitive prodrug nanoassemblies for core-shell synergistic chemo-photodynamic therapy. *Acta Biomater* 2019;**92**: 219−28.
32. Luo C, Sun B, Wang C, Zhang X, Chen Y, Chen Q, et al. Self-facilitated ROS-responsive nanoassembly of heterotypic dimer for synergistic chemo-photodynamic therapy. *J Control Release* 2019;**302**: 79−89.
33. Trott O, Olson AJ. AutoDock Vina: improving the speed and accuracy of docking with a new scoring function, efficient optimization, and multithreading. *J Comput Chem* 2010;**31**:455−61.
34. Cheng M, Cui YX, Wang J, Zhang J, Zhu LN, Kong DM. G-quadruplex/porphyrin composite photosensitizer: a facile way to promote absorption redshift and photodynamic therapy efficacy. *ACS Appl Mater Interfaces* 2019;**11**:13158−67.
35. Nam Y, Shin T, Park H, Magyar A, Choi K, Fantner G, et al. Virus-templated assembly of porphyrins into light-harvesting nanoantennae. *J Am Chem Soc* 2010;**132**:1462−3.
36. Oh JM, Choi SJ, Kim ST, Choy JH. Cellular uptake mechanism of an inorganic nanovehicle and its drug conjugates: enhanced efficacy due to clathrin-mediated endocytosis. *Bioconjugate Chem* 2006;**17**: 1411−7.
37. Zhang S, Guan J, Sun M, Zhang D, Zhang H, Sun B, et al. Self-delivering prodrug-nanoassemblies fabricated by disulfide bond bridged oleate prodrug of docetaxel for breast cancer therapy. *Drug Deliv* 2017;**24**:1460−9.
38. Goos JA, Cho A, Carter LM, Dilling TR, Davydova M, Mandleywala K, et al. Delivery of polymeric nanostars for molecular imaging and endoradiotherapy through the enhanced permeability and retention (EPR) effect. *Theranostics* 2020;**10**:567−84.